Chapter-2

2.1 Introduction

Surface plasmon resonance generation in metal surface is the origin of Raman signal in SERS resulting enhancement of local electromagnetic field, and other minor contribution is chemical enhancement (CM) via charge- transfer effect, and adsorption effect [1–2]. Coinage metals including Ag, Au and Cu are subsequently employed in the formation of SERS substrates with nanoscale size because of its significant SERS amplification and developed fabrication methods [3–6]. Among them Cu and Au exhibit plamonic resonance or interband absorption in visible wavelength region, which reduces the optimum SERS intensity [7]. On the other hand, interband absorption for Ag located in UV-visible range leads the highest SERS intensity for visible source compare to gold and copper. However, there are a number of drawbacks in traditional substrates (such as Ag, Au, and Cu) that restrict their potential, including high cost of Ag or Au, chemical instability due to oxidation of Ag or Cu, and poor biocompatibility etc. [7]. Therefore, it is necessary to acquire an alternative, facile and low-cost substrate material for Raman scattering enhancement [8]. Moreover, the semiconductor-based substrate has been recently viewed as a promising SERS substrate similar to the noble metals [9]. Numerous heterostructured non-noble metals, as well as other semiconducting oxide substrates, have shown improved effectiveness with several advantages in terms of chemical stability and biocompatibility when compared to the SERS activity of noble metals [10]. In Raman enhancement, the charge transfer mechanism is critically important [9–10] . Among the various materials, Bismuth-based substrate as an alternative non-

toxic, eco-friendly, cost-effective, plasmonic nanomaterial paved the way to choosing non-noble metal, which has attracted considerable attention due to its significant physical and chemical properties [11–13]. A non-toxic substance with photocatalytic activity, $Bi_2O_2CO_3$, is utilized to fabricate heterojunction structures to improve the optical characteristics [14].

In this work, we have synthesized $Bi_2O_2CO_3$ precursor via a facile hydrothermal method in order to investigate whether it can be a good SERS substrate or not. Further, plate-like β-Bi_2O_3/$Bi_2O_2CO_3$ heterostructures were prepared by the calcination of $Bi_2O_2CO_3$, and the formation of α-Bi_2O_3 was investigated. β-Bi_2O_3/$Bi_2O_2CO_3$heterostructure for SERS application is not reported hitherto to the best of our knowledge. The SERS performance of the heterostructure was evaluated for the primary test with the selected standard probe molecules as methyl orange (MO), rhodamine B (RhB), vitamin C (or Ascorbic acid; (Vit C)), and melamine (MEL).

Organic dyes such as MO and RhB are widely used synthetic azo-dye molecules in foods textiles etc. cause harmful effect on human health [15–17]. These dyes were selected as probe to prove the SERS activity of novel bismuth based substrate, and were studied to finding a technique of acquiring largely SERS active substrate because of weak affinity with noble molecule is challenging for SERS [15]. Moreover, bismuth based substrate was performed for the detection of Vit C and MEL to demonstrate its SERS activity for biologically important molecules such as ascorbic acid referred as vitamin C is frequently found in plants. Since human the

body cannot naturally manufacture Vit C, the excessive or insufficient control of Vit C levels indicates biological function disorder or neurological disease [18]. In addition MEL is commonly used to prepare dyes, and illegally added in dairy products, which harms kidney or potentially lethal to infants [19–20].

Further bismuth heterostucture was utilized to study the thiol group containing molecule para-aminothiophenol (PATP). PATP can readily interact with a metal substrate and exhibit highly effective SERS signals, resulting in a crucial probe molecule for SERS [21]. In addition, PATP has also been utilized to prepare surfaces for use as sensors in research on the toxicity levels in human red blood cells. Besides, PATP is an organic contaminant that damages people when they consume it directly, contaminates water, and denatures proteins. Investigating the SERS spectrum of PATP is necessary to comprehend toxicity [22]. According to experimental research published in the literature, b2 modes PATP transforms into the a_g modes (1140, 1390, and 1432 cm^{-1}) of aromatic azo molecule 4,4′-dimercaptoazobenzene (DMAB) via a surface catalytic process when adsorbed on noble metals [21]. It is well known that in SERS, EM and CMcontribute to enhancement in the Raman signal, and Haung et al. demonstrated the charge transfer enhancement effect or chemical transformation for PATP on Ag and Au [23].

2.2 Experimental section

2.2.1 Materials used

Bi $(NO_3)_3 \cdot 5H_2O$, Urea (SRL), melamine, p-aminothiophinol (Alfa Aesar), ethylene glycol, methyl orange, vitamin C, rhodamine B, and absolute ethanol all were purchased from Merck, India. All chemicals were of analytical grade reagents and used without further purification. Double distilled water was used for preparation of all aqueous solutions used in this experiment.

2.2.2 Synthesis of β-Bi_2O_3/$Bi_2O_2CO_3$

Hydrothermal method was utilized to synthesize $Bi_2O_2CO_3$ or bismuth heterostructures. In a typical procedure, 4.1 mmol of Bi $(NO_3)_3.5H_2O$ was dissolved in 40 mL ethylene glycol, and 41.6 mmol of urea was dissolved in 30 ml distilled water. Both solutions were mixed in a 100 mL beaker with stirring for 15 min. After that the solution was transferred into a Teflon-lined stainless steel autoclave and maintained at 150 ºC for 22 h, and cooled to room temperature. The resulting white precipitate ($Bi_2O_2CO_3$) was collected by centrifugation, washed with distilled water and ethanol several times and dried at 100 ºC for 12 h. The synthesized precursor was calcined at 350 ºC for 2 h with heating rate of 10 ºC in a muffle furnace for the formation of β -Bi_2O_3/$Bi_2O_2CO_3$ heterostructure. The α-Bi_2O_3/$Bi_2O_2CO_3$ and pure α-Bi_2O_3 were also prepared through calcination of precursor at 400 and 500 ºC for 2h, respectively based on the previous report with modified procedure [12].

2.2.3 Characterization

The prepared samples were characterized through several techniques, and the details are discussed in section 1.6 of chapter 1.

2.2.4 Raman measurement

MO, Vit C, RhB, MEL, and PATP were selected as SERS probe molecules. The selected analytes were measured in the concentration range of MO from 1mM to 25 µM, Vit C from 25 mM to 10 mM, MEL 25 mM, all in their aqueous form and ethanolic solution of RhB 100 µM, 10 mM to 1mM, PATP. The prepared bismuth heterostructure substrates were added into the 100 µL aqueous or ethanolic solution of probe molecule for 2 h. After that the mixed solution was dried onto the glass slide at room temperature and subjected to Raman spectroscopic measurements.

A 785 nm diode laser was used as an excitation source for the Raman and SERS measurements of all samples and 0.51 mW to 0.71 mW laser power on samples with integration time 20 s (for RhB, 5s) was used. In addition, 532 nm laser source was used for the Raman study of substrates and instrumental details are discussed in chapter 1, section 1.6.6.

2.3 Results and discussion

2.3.1 XRD pattern

Formation of $Bi_2O_2CO_3$ and β-Bi_2O_3 phase as-synthesized samples confirmed X-ray diffraction pattern (XRD) as shown in **Figure 2.1 (a-b)**. The diffraction peaks of the precursor ($Bi_2O_2CO_3$) is displayed at 2θ (in degree) = 12.9, 23.9, 26.0, 30.2, 32.7, 35.3, 39.5, 42.2, 46.9, 52.2, 53.4, 56.9, which are indexed as (002), (011), (004), (013), (110), (112), (006), (114), (020), (116), (121), (123) planes respectively of tetragonal $Bi_2O_2CO_3$ (JCPDS no. 41-1488). The intensity of

the diffraction peaks of $Bi_2O_2CO_3$ gradually decreased after two hours of calcination at 350 ºC, and some new peaks of β-Bi_2O_3 appeared at 2θ values (in degree) 27.9, 31.7, 32.7, 46.2, 54.2, 55.5, 57.8 are assigned to the (201), (002) (220), (222), (203), (421), (402) planes respectively, which are in good agreement with JCPDS card no. 27-0050 for tetragonal phase. The precursor was further calcined at 400 and 500 ºC for two hours, resulting in the formation of α-Bi_2O_3/$Bi_2O_2CO_3$ (**Figure 2.1 (c)**), and pale yellow α-Bi_2O_3, respectively. The product formation of monoclinic α-Bi_2O_3 pure phase is shown in the associated XRD pattern with diffraction planes (002), (120), (012) which intensity increases as temperature increases from 400 to 500 ºC (JCPDS file No. 41-1449), (**Figure 2.1 (d)**). The strong and sharp reflection peaks demonstrate the crystalline nature of the as-prepared samples, which are consistent with the previously reported by Selvamani et al. stable α or β-phases of Bi_2O_3prepared through thermal treatment of $Bi_2O_2CO_3$precursor [12]. In the current study as stated in the above section 2.2.2, heterostructures of α or β- Bi_2O_3/ $Bi_2O_2CO_3$ were prepared as opposed to a single α or β-Bi_2O_3.

The average crystalline size of different phases of the as-prepared samples $Bi_2O_2CO_3$,β-Bi_2O_3/ $Bi_2O_2CO_3$, α-Bi_2O_3/ $Bi_2O_2CO_3$, α-Bi_2O_3 were estimated to be 24.7, 21.1, 21.4, and 34 nm using the Scherrer equation as explained by equation 1.20 in chapter 1 section 1.6.1 [24].

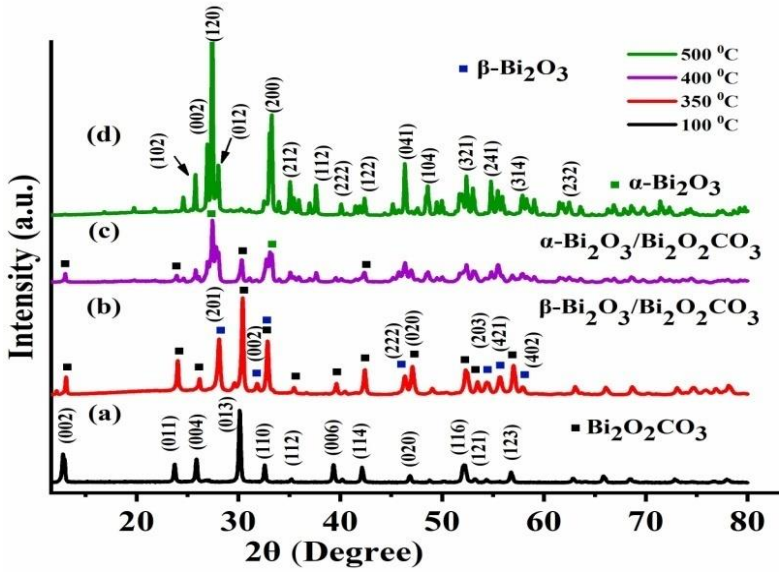

Figure 2.1 *XRD pattern of as-prepared samples: (a) $Bi_2O_2CO_3$ precursor after annealing at different temperature (b) 350 ºC (c) 500 ºC.*

2.3.2 SEM analysis

The surface morphology of the synthesized sample was characterized by a scanning electron microscope (SEM). **Figure 2.2 (a)**, shows a uniform flake-like morphology of $Bi_2O_2CO_3$ at 100 ºC with an average size about 300-400 nm, and **Figure 2.2 (b)** had plate-like structure after calcination at 350 ºC with the diameter size of the particles are in the range of 200-250 nm. At higher temperature, the image of α-$Bi_2O_3/Bi_2O_2CO_3$ exhibits an irregular size of 200-300 nm, whereas α-Bi_2O_3 shows plate like morphology with large size of near 600 nm as displayed in **Figure 2.2 (c)** and **(d)**, respectively. The change in morphology of the prepared samples during the annealing process may be due to the decomposition of $Bi_2O_2CO_3$ [25].

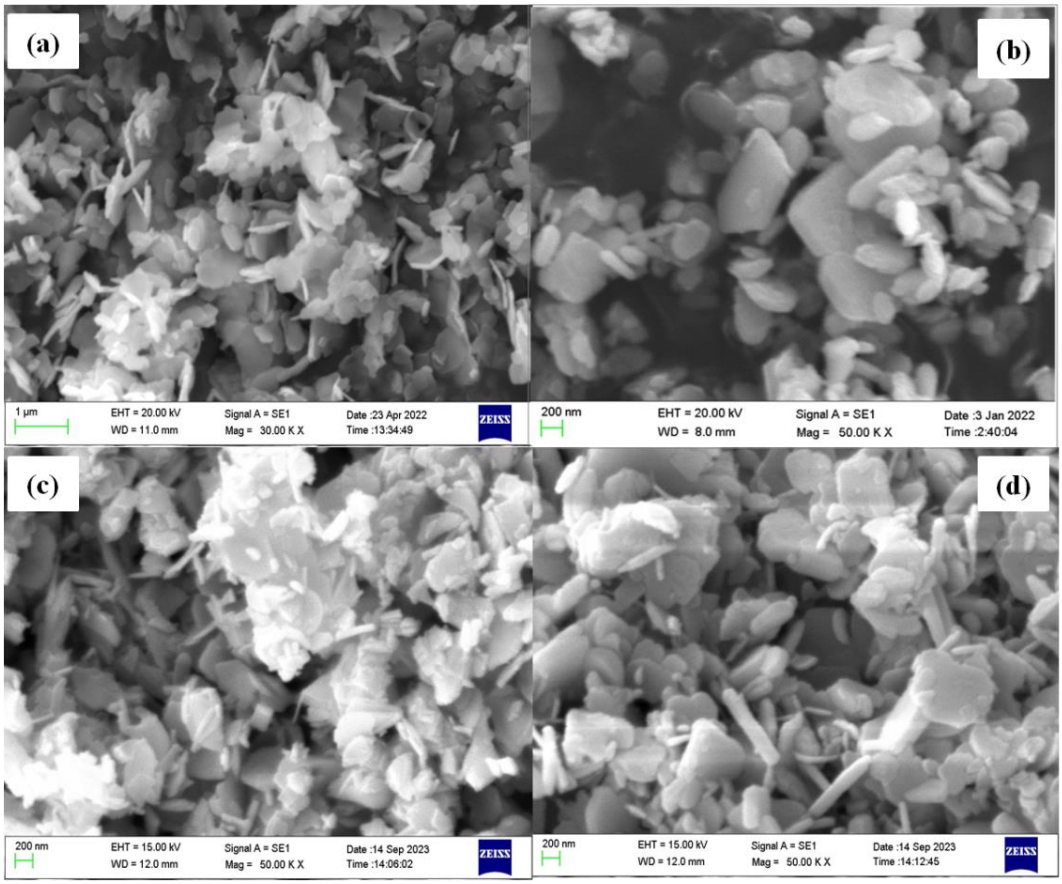

Figure 2.2 *SEM images of as-synthesized nanoparticles (a) $Bi_2O_2CO_3$,(b) β-Bi_2O_3/$Bi_2O_2CO_3$, (c) α-Bi_2O_3/ $Bi_2O_2CO_3$, (d) α-Bi_2O_3.*

2.3.3 XPS analysis

As shown in **Figure 2.3**, the survey and high-resolution XPS were carried out to elucidate the surface chemical states and elemental compositions of the bismuth heterostructure (β-Bi_2O_3/$Bi_2O_2CO_3$) at 350 ºC. **Figure 2.3 (A)** depicts the survey spectrum of bismuth heterostructure, which confirmed that elements includingbismuth, oxygen, and carbon are present. The XPS spectrum of Bi 4f with binding energy at 158.70 eV and 164.01 eV, which can be assigned to Bi $4f_{7/2}$ and

Bi $4f_{5/2}$, respectively as shown in **Figure 2.3 (B)** [26]. This indicates the Bi^{3+} chemical state in the prepared sample. **Figure 2.3 (C)** display that O1s peak at 530.1eV is attributed to Bi-O bonds, and the other peaks at 529.3 and 530.7 eV correspond to C-O in CO_3^{2-} and adsorbed water on the surface [27-28]. C1s spectrum in which the peaks at 284.5 and 288.4 eV are attributed to adventitious carbon species and CO_3^{2-} ion in $Bi_2O_2CO_3$, respectively as shown in **Figure 2.3 (D)** [29]. These results are in good accordance with the XRD analysis.

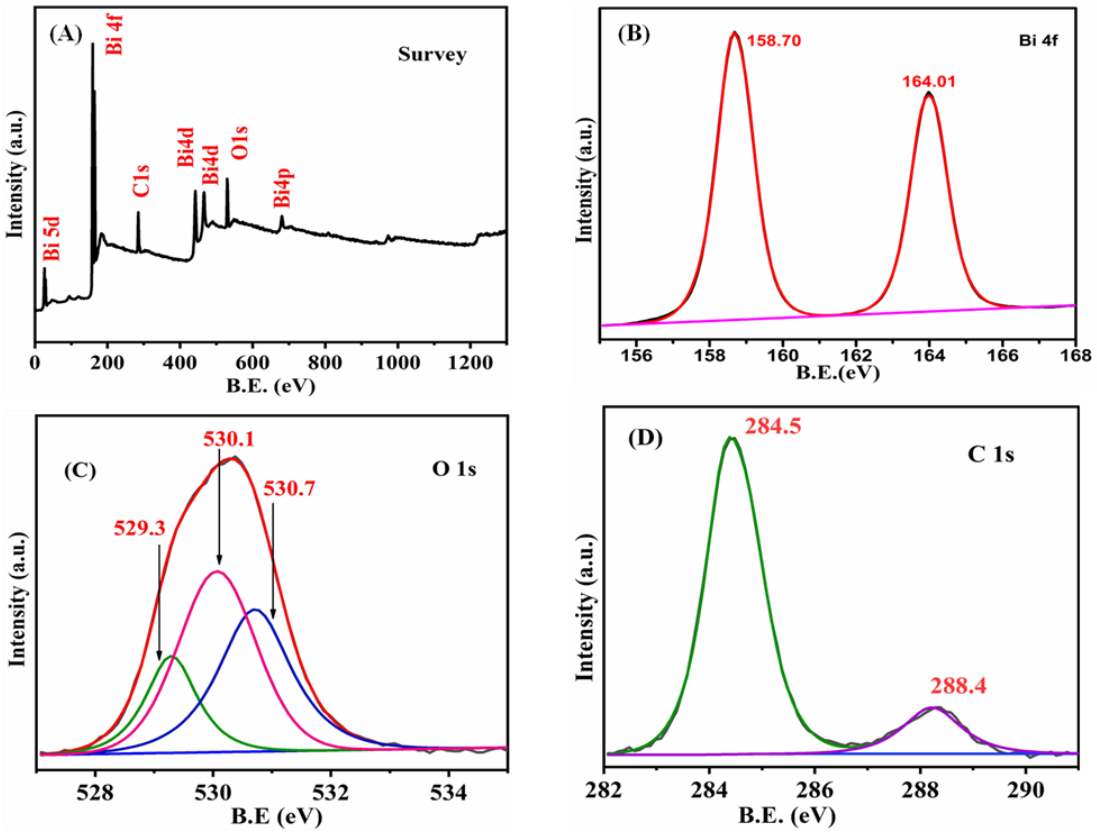

Figure 2.3 *XPS spectra for β- Bi_2O_3/$Bi_2O_2CO_3$ composites calcined at 350 ºC (A) survey spectrum and high resolution spectrum for (B) Bi 4f, (C) O 1s, (D) C 1s.*

2.3.4 Vibrational spectra of the as-synthesized samples

The recorded vibrational spectra of the as-synthesized samples are depicted in **Figure 2.4** and **Figure 2.5**. To identify the functional group present in β-Bi_2O_3/$Bi_2O_2CO_3$ nanoparticles, FT-IR analysis was performed. The symmetric stretching mode (v_1) at 1067 cm^{-1} with the sharp peak (1391 cm^{-1}) and shoulder peak (1458 cm^{-1}) for anti-symmetric vibration modesv_3 of carbonate ion (CO_3^{2-}) are shown **Figure 2.4**. The peak at 845 cm^{-1} is attributed to the out-of-plane bending mode (v_2) of carbonate ion, and the peak at 594 cm^{-1} can be assigned to the Bi-O bonds of BiO_6 units. The peak broadening at 3445 cm^{-1} is ascribed to the –OH stretching mode of the water molecule [29–31].

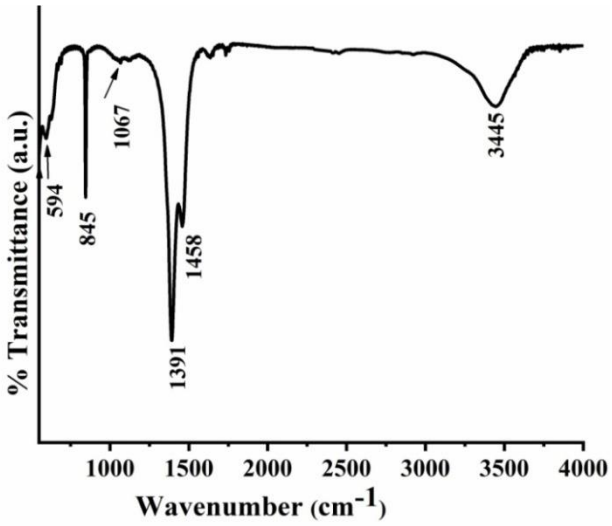

Figure 2.4 *FT-IR spectra of β-Bi_2O_3/$Bi_2O_2CO_3$ heterostructure.*

Furthermore, vibrational modes and different phases of the prepared samples were confirmed by Raman analysis with different excitation sources at 785 and 532 nm. Raman spectrum of the precursor ($Bi_2O_2CO_3$) at 785 nm with different

temperature 350, 400, and 500 ºC are shown in **Figure 2.5 (a-c)**. **Figure 2.5 (a)** demonstrate that observed Raman bands at 665, 1065 (strong), 1364 (and 1394 cm^{-1}) and 1694 cm^{-1} are ascribed to v_4, v_1, v_3, and $2v_2$ mode of CO_3^{2-} respectively for $Bi_2O_2CO_3$ [32]. In the FTIR spectra, the vibrational modev_4 is absent, which indicate that v_4 mode is only Raman active. The Raman peak at 466 cm^{-1} is attributed to the Bi-O stretching bond of β -phase of Bi_2O_3 [33]. In addition, it was noticed that as temperature increase from 350 to 500 ºC the vibrational peaks of the carbonate ion greatly decreased. When compared to the α -phase of bismuth oxide, as shown in **Figure 2.5 (c-d)**, the β -phase of bismuth oxide exhibits a red shift at 466 cm^{-1}, as displayed in **Figure 2.5 (b)**. These change in the Raman spectrum resulting from the phase transformation (from β to α-Bi_2O_3), consistent with XRD results. As shown in **Figure 2.5 (c)** at 500 ºC, the carbonate peaks of $Bi_2O_2CO_3$ disappeared, and no significant change in the position of the peak at 450 cm^{-1} was found. The strong Raman peak at 450 cm^{-1} and a shoulder at 524 cm^{-1} attributed to the displacement of an oxygen atom with respect to the Bismuth atom confirmed the formation of pure phase of α-Bi_2O_3 [34]. Furthermore, the new peak at 956 cm^{-1} in **Figure 2.5 (c)** was consistently observed but could not be assigned to any specific modes besides speculating it to be the overtone of the carbonate peak.

Moreover, to provide an evidence for the presence of $Bi_2O_2CO_3$ and α or β -Bi_2O_3 phase in samples, laser-dependent Raman analysis of bismuth heterostructures were performed at 532 nm excitation source (**Figure 2.5 (d-g)**). The peak position and intensity in the Raman spectrum were affected by the different

laser excitation source compared to 785 nm source. As shown in **Figure 2.5 (d)**, the observed characteristic Raman peaks of the precursor $Bi_2O_2CO_3$ (100 ºC) at 507, 665, 1065, 1364, 1394, and 1694 cm^{-1} again verified the FTIR as well as results obtained at 785 nm laser source (**Figure 2.5 (a)**).

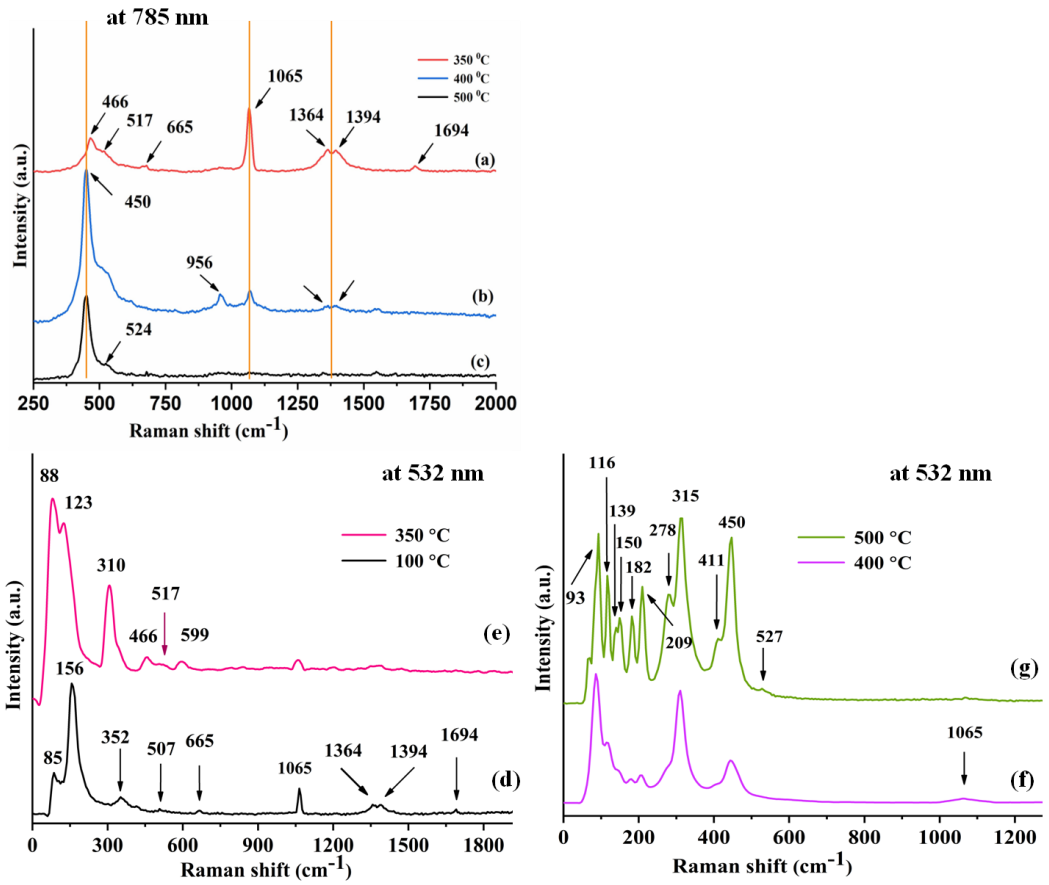

Figure 2.5 *Raman spectra of $Bi_2O_2CO_3$ precursor after annealing at different temperature (a) 350 °C (b) 400 °C (c) 500 °C at 785 nm excitation source, and $Bi_2O_2CO_3$ (d) 100, (e) 350°C (f) 400, (g) 500 °C at 532 nm excitation source.*

Other peaks at 85, 156, 352 cm^{-1} arise due to external vibration [35]. In **Figure 2.5 (e)**, the sharp peak at 88 cm^{-1}, tentatively attributed to A_{1g} vibration mode of Bi in

Bi_2O_3, and the characteristic Raman peaks at 123, 310, 466 cm^{-1} are assigned to the stretching mode of Bi-O for tetragonal phase of β-Bi_2O_3 [33]. With 532 nm excitation, the peak at 599 cm^{-1}, which corresponds to the vibrational modes of the carbonate ion, shows a comparatively higher intensity [36]. The intensity of the peak at 1065 cm^{-1} appeared significantly decreased in the Raman spectra with 532 nm excitation [12]. Likewise, **Figure 2.5 (f)** and **Figure 2.5 (g)** confirmed α-Bi_2O_3 phase at 400 ºC in α -Bi_2O_3/$Bi_2O_2CO_3$ heterostructure and 500 ºC and found that the intensity of α- Bi_2O_3 increases with increase in temperature. The peaks at 93,182, 209, 278, 315, 411, 450, and 527 cm^{-1} are the characteristic peaks of monoclinic phase of α- Bi_2O_3. The peak at 116 cm^{-1} ascribed to the displacement of oxygen atom with respect to Bi atom due to Bi-O elongation and the Raman peak at 139, 150 cm^{-1} arises due to stretching mode of Bi-O [37].

2.3.5 SERS analysis

MO, RhB, Vit C, and MEL were selected as standard probe molecules in order to demonstrate the SERS effect of the as-synthesized bismuth-based substrate bismuth heterostructure (β-Bi_2O_3/$Bi_2O_2CO_3$ nanoparticles). In order to comprehend the peak positions of each of these molecules, Raman spectra of solid MO, RhB, Vit C, and MEL were recorded. Additionally, Raman spectra of MO, Vit C, MEL solution in water, and RhB in ethanol were collected for comparison with their respective SERS spectra. **Figure 2.6**, **Figure 2.7**, **Figure 2.8**, and **Figure 2.9** display the SERS spectra of several analytes on bismuth heterostructure substrate. A 785 nm laser excitation was used to carry out the SERS investigation of MO

molecules adsorbed on β-Bi_2O_3/$Bi_2O_2CO_3$ substrates. Similar to this, SERS spectra of RhB, Vit C, and MEL were observed as demonstrated in **Figure 2.7**, **Figure 2.8**, **Figure 2.9** and corresponding spectral features of characteristic peaks are listed in **Table 2.1**.

Raman signal of aqueous MO with characteristic peaks are shown in **Figure 2.6 (a)**. **Figure 2.6 (b)** represents the SERS spectrum of MO from 1mM to 50 µM on β-Bi_2O_3/$Bi_2O_2CO_3$ nanoparticles with prominent peaks. Vibrational mode at 1118 $cm^{-1}$is attributed to stretching vibration of Ph–N. The Raman peaks at 1364, 1392 and 1419, 1445 and 1592 cm^{-1} are assigned to C–C and Ph–N stretching vibrations, N=N stretching vibration, C–C stretching vibration, respectively. The strong Raman peak of aqueous MO appeared at 1151 is shifted to 1143 cm^{-1} in the SERS spectrum attributed to C–H bending, suggesting that MO dye was adsorbed on the substrate. As shown in **Figure 2.6 (b)**, the Raman peaks, confirms that MO adsorbed on bismuth heterostructure shows enhanced SERS activity. The observed results match appreciably well with earlier reports in the literature [15–16]. Strong intensity of Raman signals was observed at higher MO concentrations, indicating increased SERS activity as a result of the increased adsorption of molecules on the substrate. The Raman signal of MO was detected at concentrations as low as 20 µM, which is close to the amplification peaks of the Raman signal at concentration of 25 µM on Ag colloids reported by Si, M.Z. et al. [15].

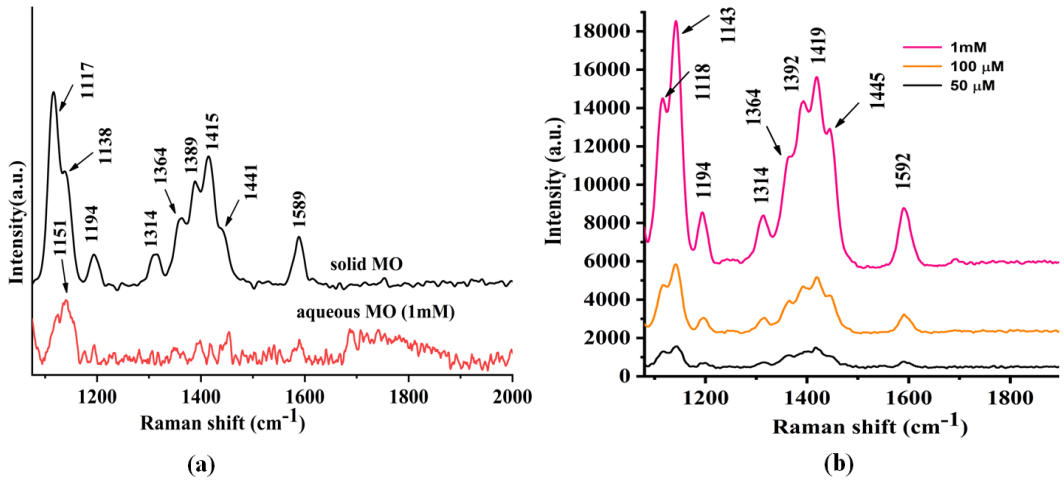

Figure 2.6 *(a) Raman spectra of aqueous (1mM) MO (b) Raman spectra of MO at different concentration from 1mM to 50 µM on Bismuth heterostructure.*

The SERS activity of the prepared substrate bismuth heterostructure was further assessed using another standard probe namely RhB. **Figure 2.7 (a)** display the measured Raman spectrum of pure RhB and its solution in ethanol, and the corresponding assignment of the Raman modes are shown **Table 2.1** have good agreement with the earlier reported literature. The SERS spectrum of 100 µM RhB on Bismuth heterostructure showed the significant and characteristic peaks at 1189, 1279, 1357, 1510, 1645 cm^{-1}. Peaks at 1189 and 1510 cm^{-1} corresponding to the C–C vibrational modes were blue shifted compared to the solid Raman spectrum, indicating the adsorption of RhB on the substrate [17].

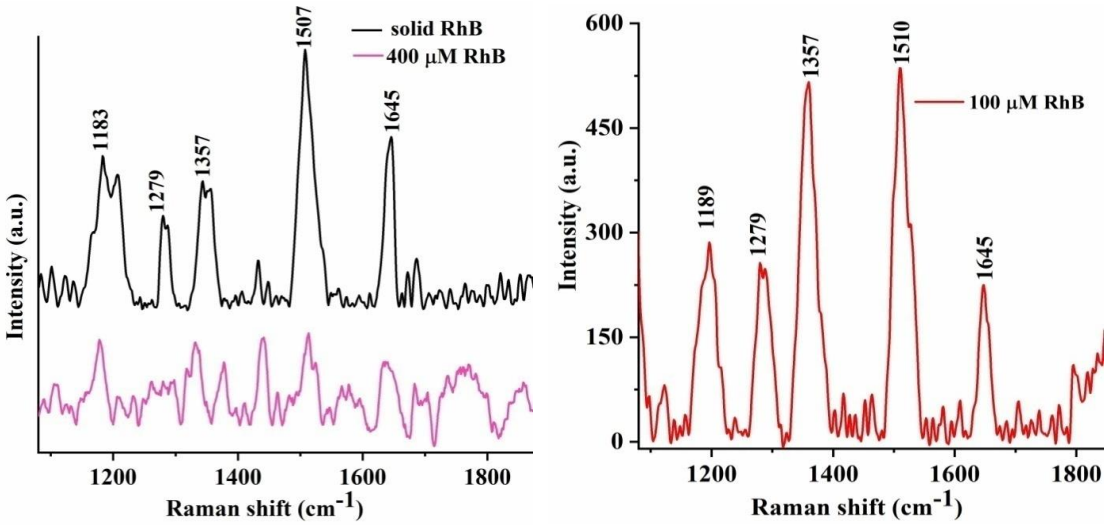

Figure 2.7 *(a) Raman spectrum of solid and 400 μM RhB in ethanol and (b) SERS spectrum of RhB in ethanol on Bismuth heterostructure at a concentration of 100 μM.*

Figure 2.8 (a) and **(b)** depict the Raman and SERS spectrum of Vit C with different concentrations from 25 mM to 10 mM adsorbed on β-Bi_2O_3/$Bi_2O_2CO_3$ nanoparticles substrate, respectively. The characteristic amplified Raman modes were observed at 1127, 1257, 1320, 1662 cm^{-1} from SERS spectra on bismuth substrate as shown in **Figure 2.8 (b)**. Three peaks from the SERS spectrum were determined to represent Vit C. The most intense Raman band at 1662 cm^{-1} corresponds to C-C ring stretching vibration, and a detailed assignment is given in **Table 2.1**. In the SERS spectrum, all the characteristic peaks were similar to the pure Raman spectrum, indicating the adsorption of Vit C on β-Bi_2O_3/$Bi_2O_2CO_3$ nanoparticles substrate and the position of the peaks in the SERS spectrum as shown in **Figure 2.8** is in good agreement with previously reported values [18].

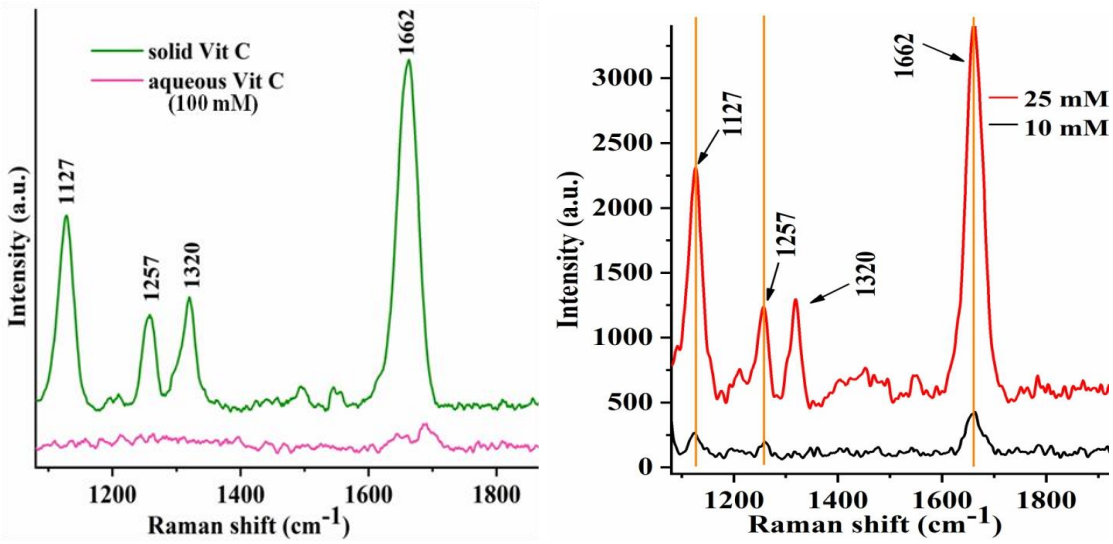

Figure 2.8 *(a) Raman spectrum of solid and 100 mM aqueous Vit C. (b) SERS spectra of Vit C. (25 mM, 10 mM) on Bismuth heterostructure substrate.*

The Raman spectrum of solid melamine (MEL) and aqueous MEL of 25 mM concentration over β-Bi_2O_3/$Bi_2O_2CO_3$ were recorded, and illustrated in **Figure 2.9 (a-b)**. The significant and characteristic Raman peaks of pure MEL were observed at 584, 675, 982, 1557 cm^{-1} associated with different modes of vibrations (**Table 2.1**). The sharp peak at 673 cm^{-1} in the SERS spectrum reveals the in-plane deformation of triazine ring (ring breathing mode II). The second prominent peak at 980 cm^{-1} was attributed to the ring-breathing mode I of the triazine ring and the Raman peak at 1554 cm^{-1} arises from bending mode of vibration of the amine group [19–20]. The shift in SERS spectrum compared to the peaks in the Raman spectrum of solid MEL is due to the interaction of MEL with the bismuth heterostructure surface.

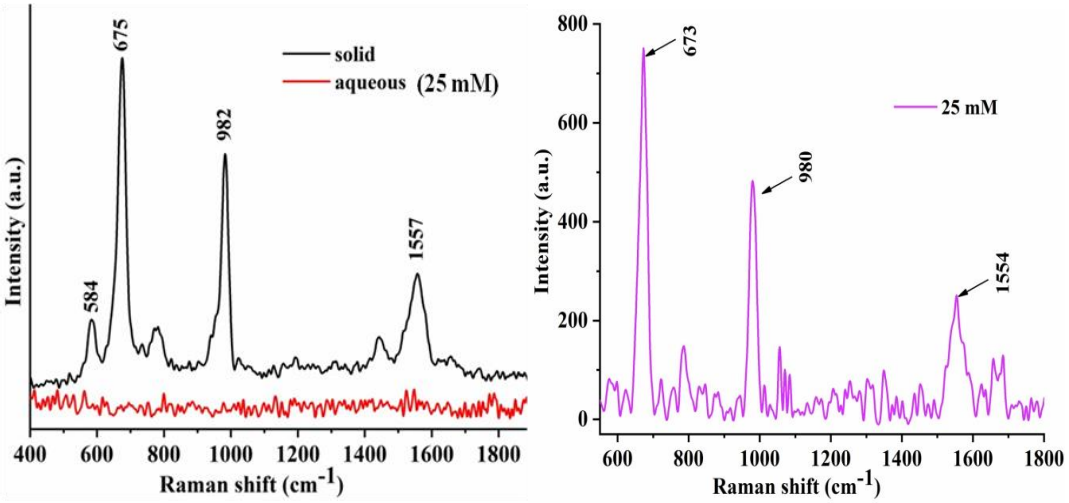

(a) **(b)**

Figure 2.9 *(a) Raman spectra of solid and 25 mM aqueous MEL (b) SERS spectra of 25 mM MEL on Bismuth heterostructure substrate.*

In addition, the effect of decomposition of $Bi_2O_2CO_3$ in the SERS performance of bismuth heterostructure substrates was demonstrated. From the XRD results it is evident that when the ratio of $Bi_2O_3/Bi_2O_2CO_3$ exceeds 0.54, the Bi_2O_3 undergoes phase transition from its β phase to α phase. The ratio was obtained by considering the most intense peak in the XRD data corresponding to each temperature as shown in **Figure 2.1**. SERS activity of $Bi_2O_3/Bi_2O_2CO_3$ nanoparticles depends upon the ratio of Bi_2O_3 to that of $Bi_2O_2CO_3$. **Figure 2.10** shows that the SERS signals (as measured from the peak intensity at 1419 cm^{-1}) of MO increases with the decomposition of $Bi_2O_2CO_3$ and reaches the highest when the ratio $Bi_2O_3/Bi_2O_2CO_3$ is 0.54. When the amount of Bi_2O_3 continuously increases as inferred from the ratio being more than 0.54, the SERS signals of MO fall to a lower intensity.

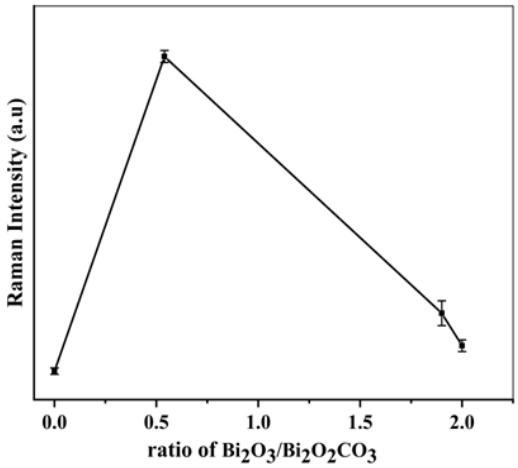

Figure 2.10 *The correlation between SERS intensity of MO at 1419 cm^{-1} and the ratio of $Bi_2O_3/Bi_2O_2CO_3$.*

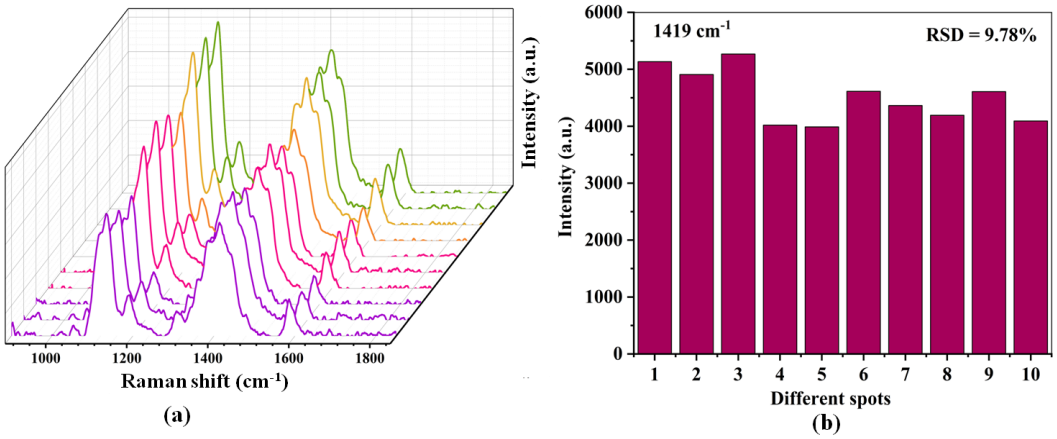

Figure 2.11 *(a) SERS spectra of MO (10^{-4} M) from randomly selected 10 spots (b) histogram for relative standard deviation (RSD) corresponding to peak 1419 cm^{-1}.*

Moreover, aqueous solution of MO with 10^{-4} M concentration was employed as a probe molecule to test the stability and reproducibility of the as-prepared substrate. SERS spectra were taken from randomly selected ten spots on β -$Bi_2O_3/Bi_2O_2CO_3$ at the same test conditions. **Figure 2.11 (a)** demonstrates that the SERS spectra are nearly identical, and relative standard deviation (RSD) around 9.78

% regarding the peak at 1419 cm^{-1} depicts the excellent signal reproducibility as shown in **Figure 2.11 (b)**.

2.3.6 SERS study of PATP

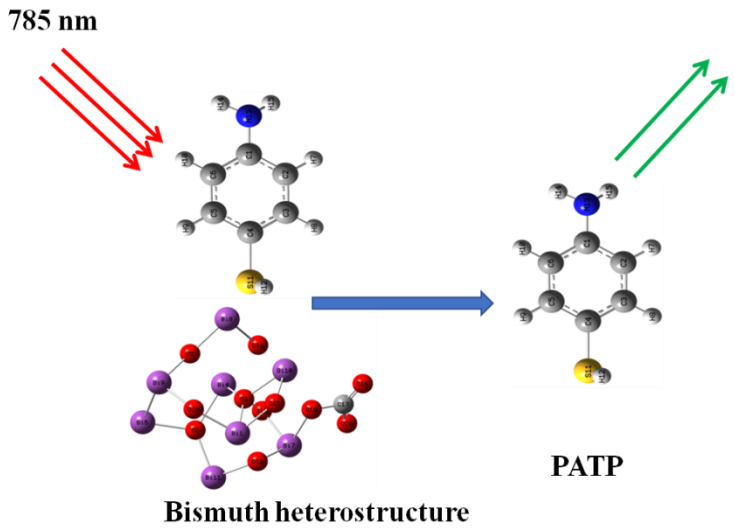

Figure 2.12 *schematic diagrams for genuine SERS of PATP on bismuth heterostructure.*

2.3.6.1 SERS of PATP on bismuth heterostructure

Spontaneous Raman spectrum of solid PATP, and 50 mM PATP in ethanol solution are displayed in **Figure 2.13 (a)**. SERS spectrum of PATP on the prepared bismuth heterostructure (β-Bi_2O_3/$Bi_2O_2CO_3$) shown in **Figure 2.13 (b)**. The normal Raman spectrum of PATP was recorded to be compared with the correlated SERS spectrum and to show the enhancement caused by the SERS substrate. The sharp peak observed at 1091 cm^{-1} arises due to stretching mode of C-S (νC–S) in PATP as

illustrated in the Raman spectrum of the solid PATP. Other peaks at 1171 cm^{-1} and 1595 cm^{-1} attributed to the bending mode of CH (δCH), and stretching mode of C-C (νCC), respectively. These results are in well agreement with previous report [21, 23, 38], and the corresponding tentative assignment of the measured Raman modes of PATP are listed in **Table 2.2**. The signature peaks of PATP on the bismuth heterostructure substrate were detected in the SERS spectrum at 630, 822, 1079, 1174, 1482 and 1590 cm^{-1} which are in accordance with the spontaneous Raman spectra of solid PATP. When compared to the Raman spectra of solid PATP, the Raman peak at 822 cm^{-1} indicates a blue shift corresponds to the C-H wagging (πCH), while the peak at 1079 cm^{-1} exhibits a red shift by 12 cm^{-1} related to C-S stretching vibration (νCS) of a_1 mode, which demonstrates the strong interaction of PATP on the bismuth-based substrate. The Raman peaks at 1174, and 1482 cm^{-1} can assign to CH bending vibration (δCH), and νCH + δCH vibrational bands of, and the peak at 1590 cm^{-1} corresponds to the C-C stretching bond (νCC) of a_1 modes. The observed results indicate that the SERS signal was detected from original molecule, and the dimerization of PATP to a_g mode of DMAB was not observed.

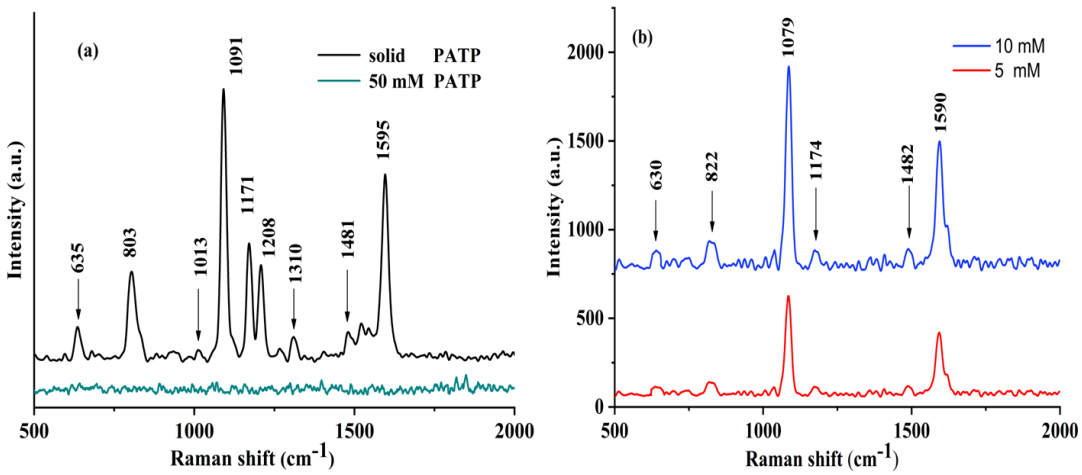

Figure 2.13 *(a) Raman spectra of solid PATP and 50 mM PATP in ethanol (b) SERS spectra of PATP (10 mM, 5 mM) on Bismuth heterostructure.*

Genuine SERS measurement of PATP

PATP dimerization into DMAB in the SERS measurement has been noticed for many decades. For example, noble metals gold and silver nanoparticles as SERS substrates were used by Huang et al. [21, 23] to study the SERS behavior of p-ATP. As a function of laser power dependence of the incident radiation during SERS studies, they observed that 4,4'-dimercaptoazobenzene (DMAB) is formed. Moreover, Arathi et al. have also demonstrated the photodimerization of PATP on copper (Cu), copper pencil graphite (Cu-PG) or Cu@Pd-PG due to the surface catalyzed reaction [39]. These studies reveal that PATP is transformed to a_g mode (1140, 1388, 1438 cm^{-1}) of DMAB (4, 4'-dimercaptoazobenzene), and the intensity of a_g modes are considerably stronger than those of a_1 mode of PATP. Compared to the aforementioned reported SERS of PATP seen on noble metal Cu, Ag or Au nanostructures, Tian et al. [40] reported the first detection of the genuine PATP

SERS spectra on Ag nanowire-Ag film system, in which the DMAB modes at 1140, 1390, and 1432 cm^{-1} were absent. Further it was observed that after increasing the irradiation time (at 60 s) continuously with 632.8 nm laser source strong Raman peaks of DMAB were appeared, and they found that by increasing the plasmonic enhancement, the chemical reaction of dimerization can proceed more quickly. Therefore, they assume that it is reasonable to the reaction duration and reaction extent can be regulated by selecting a different SERS system, altering the laser intensity, and adjusting the concentration of molecule solution. Recently Wang et al. [41] also reported genuine SERS study of PATP on Pt-based hollow nanostructures at 532 nm excitation source. The SERS spectra of PATP with a long period of illumination and varying concentrations of PATP solution were unaffected, and the vibrational modes of DMAB were not observed.

Similarly, in this study we observed the genuine SERS spectrum of PATP on bismuth heterostructure (β-Bi_2O_3/$Bi_2O_2CO_3$ nanoparticles) with different concentration range from 10^{-2} M to 10^{-3} M and laser irradiation time for 5 min at 785 nm wavelength. The SERS spectrum of PATP were seen remain intact and the dimerization of PATP into DMAB was absent. This finding reveals the genuine SERS spectrum of PATP in the SERS measurement, which is consisted with recently reported genuine SERS study of PATP on Ag based substrates or Pt-based hollow nanostructures by Tian et al and Wang et al. [40–41], respectively. Additionally, the most intense peaks of PATP supporting the idea that β-Bi_2O_3/$Bi_2O_2CO_3$ nanoparticles are a potentially effective substrate for non-invasive SERS detection

molecules.

As previously mentioned, SERS is typically explained by two mechanisms viz. EM related to the LSPR of the SERS substrate caused by the incident laser wavelength with enhancement factors up to 10 or 12 orders of magnitudes, whereas CM brought on by charge transfer between the adsorbate and the substrate [42]. The enhancement factor for molecules adsorbed on β-Bi_2O_3/$Bi_2O_2CO_3$ heterostructure can be estimated using equation 1.18 as explained [4, 42–45] in chapter 1, section 1.3.2.

The SERS enhancement in non-noble metal oxide and heterostructure is well known to be primarily controlled by chemical enhancement, with SERS factors ranging from 1 to 3 orders of magnitude [8]. It was observed that with β-Bi_2O_3/$Bi_2O_2CO_3$ nanoparticle substrate for all the analytes studied herein corresponding to the most prominent peaks. For SERS measurement 100 µL of analyte solution (100 µM for MO, RhB, 10 mM for Vit C and 25 mM for MEL, and 5mM for PATP) was deposited onto the area of 15 mm^2 on the substrate of β-Bi_2O_3/$Bi_2O_2CO_3$ nanoparticles substrate, the SERS enhancement factor of 2–3 orders of magnitude was obtained. Therefore, it is expected that with β-Bi_2O_3/$Bi_2O_2CO_3$ nanoparticles substrate it is the chemical enhancement that is dominant while giving SERS effect.

Although more experiments are required to precisely explain the enhancement mechanism for SERS in bismuth- based materials.

2.4 Conclusion

Novel SERS active bismuth heterostructured nanoparticles substrates were successfully synthesized via the hydrothermal method. As- prepared samples were examined using Raman spectroscopy, which revealed the distinctive peaks associated with the, α, β -Phase of bismuth materials as supported by XRD. We found that heat treatment causes the relative intensity of bismuth oxides to rise while the carbonate peaks in the samples fall. Inexpensive facile approach to synthesize β - $Bi_2O_3/Bi_2O_2CO_3$ substrate exhibited higher SERS activity compared to α-Bismuth based composites, which have been utilized to detect numerous chemicals and demonstrate the adsorption of analytes on a substrate and well define Raman signal for MO, RhB, VitC, and MEL. The detection limit was determined for MO 20 µM, RhB 100 µM, Vit C 10 mM, MEL 25 mM, and PATP 1mM which demonstrate the SERS activity of Bismuth heterostructure that can detect different probe molecules. The genuine SERS spectrum of PATP was obtained where dimerization of PATP into DMAB was absent. The observed enhancement factor for the considered analytes was 2-3 orders of magnitudes. In conclusion, utilizing bismuth-based materials is an important strategy for the development of a highly efficient SERS substrate.

Table 2.1 Assignment of vibrational modes of selected molecules MO, RhB, Vit C, and MEL

Analyte	**Raman shift (cm^{-1})**	**Assignment**
MO	1118 1151/1143 1364 1389/1419 1445/1592	*v* (Ph–N) *δ* (C–H) *v* (C–C) *v*(Ph–N) *v* (N=N) *v* (C–C) Ref [15], [16]
RhB	1183/1189 1279 1357, 1507/1510 1645	C−C bridge band stretching and aromatic *δ*(C−H) aromatic *δ*(C−C) aromatic *v* (C–C) Ref [17]
Vit C	1127 1257 1320 1662	*v* (C-O-C) *δ*(C-O-H) (twisting) *δ*(CH) (wagging) C=C stretching in ring Ref [18]
MEL	584 675/673 982/980 1557/1554	δ(NCN) + τ(NH_2) Ring breathing mode II Ring breathing mode I (NH_2) Ref [19], [20]

Table 2.2 Tentative assignment for Raman mode of PATP [21], [23], [38]

Raman shift (cm^{-1})	**Tentative assignment**
635	γ C-C-C
803	πC-H
1013	γ CC+ γ CCC
1091	νC-S
1171	δC-H
1310	νCC+ δ CH
1481	*ν*CC+*δ*CH
1595	νC-C

ν = stretching, δ = bending, γ = out-of-plane bending, π = wagging, Ph = phenyl group, τ = torsion

References

[1] R. A. Alvarez-Puebla and L. M. Liz-Marzán, "Traps and cages for universal SERS detection," *Chem. Soc. Rev.*, vol. 41, no. 1, pp. 43–51, 2012, doi: 10.1039/C1CS15155J.

[2] A. Campion and P. Kambhampati, "Surface-enhanced Raman scattering," *Chem. Soc. Rev.*, vol. 27, no. 4, pp. 241–250, 1998.

[3] J. Reguera, J. Langer, D. J. de Aberasturi, and L. M. Liz-Marzán, "Anisotropic metal nanoparticles for surface-enhanced Raman Scattering," *Colloid. Synth. Plasmonic Nanometals*, pp. 713–754, 2020.

[4] K. Kneipp *et al.*, "Surface-enhanced Raman spectroscopy in single living cells using gold nanoparticles," *Appl. Spectrosc.*, vol. 56, no. 2, pp. 150–154, 2002.

[5] L. Chen, J. Yu, T. Fujita, and M. Chen, "Nanoporous copper with tunable nanoporosity for SERS applications," *Adv. Funct. Mater.*, vol. 19, no. 8, pp. 1221–1226, 2009.

[6] W. Wu *et al.*, "Morphology controllable synthesis of silver nanoparticles: Optical properties study and SERS application," *J. Alloys Compd.*, vol. 579, pp. 117–123, 2013.

[7] P. R. West, S. Ishii, G. V Naik, N. K. Emani, V. M. Shalaev, and A. Boltasseva, "Searching for better plasmonic materials," *Laser Photon. Rev.*, vol. 4, no. 6, pp. 795–808, 2010.

[8] X. X. Han, W. Ji, B. Zhao, and Y. Ozaki, "Semiconductor-enhanced Raman scattering: Active nanomaterials and applications," *Nanoscale*, vol. 9, no. 15, pp. 4847–4861, 2017.

[9] P. J. Arathi, B. Seemesh, R. K. R. G., S. K. P., and V. Ramanathan, "Disulphide linkage: To get cleaved or not? Bulk and nano copper based SERS of cystine," *Spectrochim. Acta - Part A Mol. Biomol. Spectrosc.*, vol. 196, pp. 229–232, 2018, doi: 10.1016/j.saa.2018.02.010.

[10] J. Wang, F. Ma, and M. Sun, "Graphene, hexagonal boron nitride, and their heterostructures: properties and applications," *RSC Adv.*, vol. 7, no. 27, pp. 16801–16822, 2017, doi: 10.1039/C7RA00260B.

[11] Z. Wang, C. Jiang, R. Huang, H. Peng, and X. Tang, "Investigation of Optical and Photocatalytic Properties of Bismuth Nanospheres Prepared by a Facile Thermolysis Method," *J. Phys. Chem. C*, vol. 118, no. 2, pp. 1155–1160, Jan. 2014, doi: 10.1021/jp4065505.

[12] T. Selvamani, S. Anandan, L. Granone, D. W. Bahnemann, and M. Ashokkumar, "Phase-controlled synthesis of bismuth oxide polymorphs for photocatalytic applications," *Mater. Chem. Front.*, vol. 2, no. 9, pp. 1664–1673, 2018, doi: 10.1039/c8qm00221e.

[13] M. A. Shahbazi, "Faghfouri L. Ferreira MPA Figueiredo P. Maleki H. Sefat F. Hirvonen J. Santos HA Chem," *Soc. Rev*, vol. 49, pp. 1253–1321, 2020.
[14] Y. Lu *et al.*, "Oxygen vacancy engineering of $Bi_2O_3/Bi_2O_2CO_3$ heterojunctions: Implications of the interfacial charge transfer, NO adsorption and removal," *Appl. Catal. B Environ.*, vol. 231, pp. 357–367, 2018.
[15] M. Z. Si, Y. P. Kang, and Z. G. Zhang, "Surface-enhanced Raman scattering (SERS) spectra of Methyl Orange in Ag colloids prepared by electrolysis method," *Appl. Surf. Sci.*, vol. 255, no. 11, pp. 6007–6010, 2009, doi: 10.1016/j.apsusc.2009.01.055.
[16] J. Prakash *et al.*, "Optical and surface enhanced Raman scattering properties of Au nanoparticles embedded in and located on a carbonaceous matrix," *Phys. Chem. Chem. Phys.*, vol. 18, no. 4, pp. 2468–2480, 2016, doi: 10.1039/C5CP06134B.
[17] J. Zhang, X. Li, X. Sun, and Y. Li, "Surface Enhanced Raman Scattering Effects of Silver Colloids with Different Shapes," *J. Phys. Chem. B*, vol. 109, no. 25, pp. 12544–12548, Jun. 2005, doi: 10.1021/jp050471d.
[18] C. Y. Panicker, H. T. Varghese, and D. Philip, "FT-IR, FT-raman and SERS spectra of vitamin C," *Spectrochim. Acta Part A Mol. Biomol. Spectrosc.*, vol. 65, no. 3–4, pp. 802–804, 2006.
[19] N. E. Mircescu, M. Oltean, V. Chiş, and N. Leopold, "FTIR, FT-Raman, SERS and DFT study on melamine," *Vib. Spectrosc.*, vol. 62, pp. 165–171, 2012.
[20] E. Koglin, B. J. Kip, and R. J. Meier, "Adsorption and displacement of melamine at the Ag/electrolyte interface probed by surface-enhanced Raman microprobe spectroscopy," *J. Phys. Chem.*, vol. 100, no. 12, pp. 5078–5089, 1996.
[21] Y.-F. Huang, H.-P. Zhu, G.-K. Liu, D.-Y. Wu, B. Ren, and Z.-Q. Tian, "When the signal is not from the original molecule to be detected: chemical transformation of para-aminothiophenol on Ag during the SERS measurement," *J. Am. Chem. Soc.*, vol. 132, no. 27, pp. 9244–9246, 2010.
[22] P. Amrolia, S. G. Sullivan, A. Stern, and R. Munday, "Toxicity of aromatic thiols in the human red blood cell," *J. Appl. Toxicol.*, vol. 9, no. 2, pp. 113–118, 1989.
[23] Y.-F. Huang *et al.*, "Surface-enhanced Raman spectroscopic study of p-aminothiophenol," *Phys. Chem. Chem. Phys.*, vol. 14, no. 24, pp. 8485–8497, 2012.
[24] B. D. Cullity, *Elements of X-ray Diffraction*. Addison-Wesley Publishing, 1956.
[25] H.-Y. Jiang, P. Li, G. liu, J. Ye, and J. Lin, "Synthesis and photocatalytic properties of metastable β-Bi_2O_3 stabilized by surface-coordination effects," *J. Mater. Chem. A*, vol. 3, no. 9, pp. 5119–5125, 2015, doi: 10.1039/C4TA06235C.
[26] G. Zhu, J. Lian, M. Hojamberdiev, and W. Que, "Facile fabrication of porous Bi 2 O 3 microspheres by thermal treatment of Bi 2 O 2 CO 3 microspheres and its photocatalysis properties," *J. Clust. Sci.*, vol. 24, pp. 829–841, 2013.
[27] S. Shamaila, A. K. L. Sajjad, F. Chen, and J. Zhang, "Study on highly visible light

active Bi_2O_3 loaded ordered mesoporous titania," *Appl. Catal. B Environ.*, vol. 94, no. 3–4, pp. 272–280, 2010.
[28] N. Liang *et al.*, "Highly efficient Ag2O/Bi2O2CO3 pn heterojunction photocatalysts with improved visible-light responsive activity," *ACS Appl. Mater. Interfaces*, vol. 6, no. 14, pp. 11698–11705, 2014.
[29] L. Chen, R. Huang, S.-F. Yin, S.-L. Luo, and C.-T. Au, "Flower-like Bi2O2CO3: Facile synthesis and their photocatalytic application in treatment of dye-containing wastewater," *Chem. Eng. J.*, vol. 193, pp. 123–130, 2012.
[30] F. Dong, Y. Sun, M. Fu, W.-K. Ho, S. C. Lee, and Z. Wu, "Novel in situ N-doped (BiO) 2CO3 hierarchical microspheres self-assembled by nanosheets as efficient and durable visible light driven photocatalyst," *Langmuir*, vol. 28, no. 1, pp. 766–773, 2012.
[31] V. Dimitrov, Y. Dimitriev, and A. Montenero, "IR spectra and structure of V2O5□ GeO2□ Bi_2O_3 glasses," *J. Non. Cryst. Solids*, vol. 180, no. 1, pp. 51–57, 1994.
[32] P. Taylor, S. Sunder, and V. J. Lopata, "Structure, spectra, and stability of solid bismuth carbonates," *Can. J. Chem.*, vol. 62, no. 12, pp. 2863–2873, 1984.
[33] F. D. Hardcastle and I. E. Wachs, "The molecular structure of bismuth oxide by Raman spectroscopy," *J. Solid State Chem.*, vol. 97, no. 2, pp. 319–331, 1992.
[34] M. Ahila, M. Malligavathy, E. Subramanian, and D. P. Padiyan, "Controllable synthesis of α and β-Bi_2O_3 through anodization of thermally evaporated bismuth and its characterization," *Solid State Ionics*, vol. 298, pp. 23–34, 2016.
[35] G. E. Tobón Zapata, S. B. Etcheverry, and E. J. Baran, "Vibrational spectrum of bismuth subcarbonate," *J. Mater. Sci. Lett.*, vol. 16, 1997.
[36] H. Lu, L. Xu, B. Wei, M. Zhang, H. Gao, and W. Sun, "Enhanced photosensitization process induced by the p–n junction of Bi2O2CO3/BiOCl heterojunctions on the degradation of rhodamine B," *Appl. Surf. Sci.*, vol. 303, pp. 360–366, 2014.
[37] V. N. Denisov, A. N. Ivlev, A. S. Lipin, B. N. Mavrin, and V. G. Orlov, "Raman spectra and lattice dynamics of single-crystal," *J. Phys. Condens. Matter*, vol. 9, no. 23, p. 4967, 1997.
[38] M. Osawa, N. Matsuda, K. Yoshii, and I. Uchida, "Charge transfer resonance Raman process in surface-enhanced Raman scattering from p-aminothiophenol adsorbed on silver: Herzberg-Teller contribution," *J. Phys. Chem.*, vol. 98, no. 48, pp. 12702–12707, 1994.
[39] P. J. Arathi, S. Bhaskar, G. Rajendra Kumar Reddy, P. Suresh Kumar, and V. Ramanathan, "The photocatalytic role of electrodeposited copper on pencil graphite," *Phys. Chem. Chem. Phys.*, vol. 20, no. 5, pp. 3430–3432, 2018, doi: 10.1039/c7cp08383a.
[40] X. Tian, L. Chen, H. Xu, and M. Sun, "Ascertaining genuine SERS spectra of p-

aminothiophenol," *Rsc Adv.*, vol. 2, no. 22, pp. 8289–8292, 2012.
[41] Y. Wang *et al.*, "Pt-based nanostructures for observing genuine SERS spectra of p-aminothiophenol (PATP) molecules," *Appl. Sci.*, vol. 7, no. 9, p. 953, 2017.
[42] E. C. Le Ru, E. Blackie, M. Meyer, and P. G. Etchegoin, "Surface enhanced Raman scattering enhancement factors: a comprehensive study," *J. Phys. Chem. C*, vol. 111, no. 37, pp. 13794–13803, 2007.
[43] A Saroj, U Sharma, S Das, V Ramanathan, "Bismuth based novel substrate for surface enhanced Raman spectroscopy" *Spectrochim. Acta - Part A Mol. Biomol. Spectrosc.*, vol. 280, pp. 121576, 2022, doi: 10.1016/j.saa.2022.121576.
[44] J. K. Kim and D.-J. Jang, "Hollow and inward-bumpy gold nanoshells fabricated using expanded silica mesopores as templates," *New J. Chem.*, vol. 43, no. 24, pp. 9732–9739, 2019.
[45] P Bhadoria, A Saroj, V Ramanathan, "To dimerize or not: para-aminothiophenol on a bismuth heterostructure." *Phys. Chem. Chem. Phys.*, vol. 25, pp. 9569-9575, 2022, doi: 10.1039/D2CP05918E.